THE JOURNAL OF PHYSICAL CHEMISTRY LETTERS
A JOURNAL OF THE AMERICAN CHEMICAL SOCIETY

pubs.acs.org/JPCL Letter

Interface-Induced Conservation of Momentum Leads to Chiral-Induced Spin Selectivity

Clemens Vittmann, R. Kevin Kessing, James Lim, Susana F. Huelga, and Martin B. Plenio*

Cite This: J. Phys. Chem. Lett. 2022, 13, 1791−1796 Read Online

ACCESS | Metrics & More | Article Recommendations | Supporting Information

ABSTRACT: We study the nonequilibrium dynamics of electron transmission from a straight waveguide to a helix with spin−orbit coupling. Transmission is found to be spin-selective and can lead to large spin polarizations of the itinerant electrons. The degree of spin selectivity depends on the width of the interface region, and no polarization is found for single-point couplings. We show that this is due to momentum conservation conditions arising from extended interfaces. We therefore identify interface structure and conservation of momentum as crucial ingredients for chiral-induced spin selectivity, and we confirm that this mechanism is robust against static disorder.

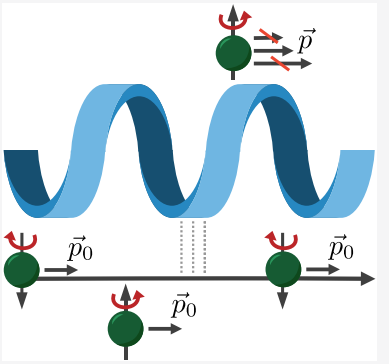

Chiral-induced spin selectivity (CISS)[1,2] is an intriguing phenomenon wherein the chirality of organic molecules such as DNA,[3] oligopeptides,[4] bacteriorhodopsine,[5] or photosystem I[6] induces notable spin dependence on various electronic processes. Experiments have demonstrated that unpolarized photoelectrons can become highly spin-polarized when transmitted through (mono)layers of helical molecules, with the molecule's handedness deciding the sign of the polarization.[7,8] The CISS effect has also been observed for bound electron transport in the form of spin-dependent currents when helical molecules are placed between a substrate and an atomic force microscope (AFM) tip.[9] Naturally, such phenomena have attracted much interest in the field of spintronics that uses the electron spin to process information in nanodevices.[10−15] More recently, the relations between electron spin, enantioselectivity and chemical reactivity in chiral molecules has also been the subject of increased attention.[16−20] Though it is apparent that the experimentally observed spin polarization is related to the spin−orbit coupling (SOC) experienced by the electrons moving through the helical or chiral structures,[21−30] a consensus on the microscopic mechanism has not yet been reached.[31]

In this work, we present a simple and natural model exhibiting CISS whose underlying mechanism can be rigorously understood using intuitive physical concepts: Electrons initially traveling along a SOC-free straight waveguide approach a helical waveguide (Figure 1a) with SOC to which they can tunnel, resulting in an effective coupling region of width ξ (Figure 1b). We show that an initially spin-unpolarized electron wavepacket naturally becomes polarized after coming into proximity with the helix *if* the interaction region is not a single point, i.e., if $\xi > 0$. This process can be repeated if the electron then comes into contact with further helices, amplifying the effect. We demonstrate that high spin polarization ∼50% can be achieved for moderate SOC strengths $\hbar\alpha \sim 1$ meV nm, despite the helical waveguide being modeled as a single one-dimensional channel without—contrary to previous theoretical studies—intramolecular multichannel structures. However, when the SOC-free and helical waveguides are coupled only at a single point ($\xi \to 0$), the outgoing state remains unpolarized. As we will show in this work, these results can be rationalized in terms of spin-dependent interwaveguide transmission probabilities, as an extended interaction region $\xi > 0$ prescribes (partial) conservation of momentum, resulting in spin-selective transmissions due to spin−orbit coupling within the helix. Therefore, our work highlights the importance of interface modeling in CISS.

As shown in Figure 1a, each helical molecule is characterized by its radius R and pitch $2\pi P$; we use the geometrical parameters of DNA, R = 0.7 nm and $2\pi P$ = 3.4 nm,[32] throughout. As a model for an electron traveling through the potential energy landscape of a helical molecule, we assume that an electron wavepacket propagates solely in the tangential direction $\mathbf{e}_T$ of a helical path due to a trapping potential acting in the normal $\mathbf{e}_N$ and binormal $\mathbf{e}_B$ directions. The electron's

Received: December 7, 2021
Accepted: February 11, 2022
Published: February 16, 2022

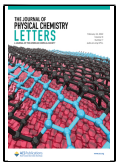

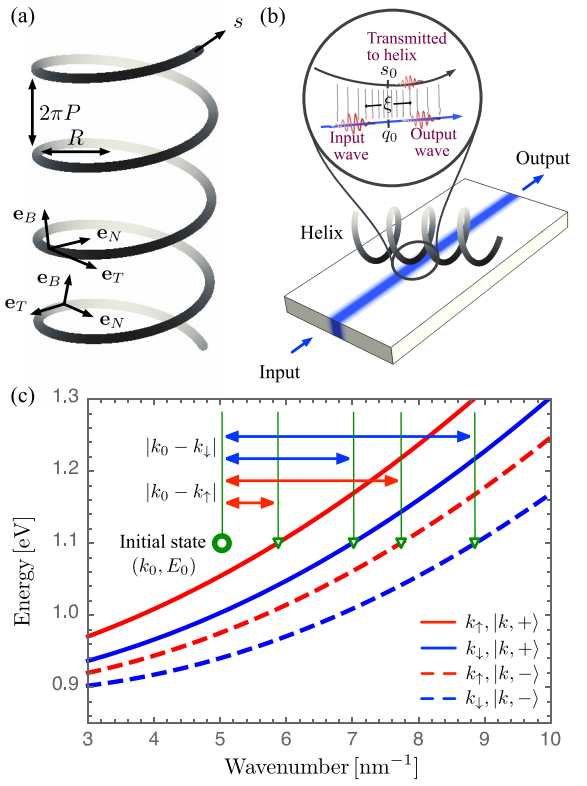

Figure 1. (a) Helix-shaped waveguide with radius R and pitch $2\pi P$. At each point, a coordinate system is defined by the normal ($\mathbf{e}_N$), binormal ($\mathbf{e}_B$), and tangential ($\mathbf{e}_T$) vectors. (b) Schematic representation of an electron wavepacket traveling along a straight SOC-free waveguide being scattered off a nearby helical waveguide. The scattering occurs over a region of nonzero length ξ, leading to a transmitted wavepacket in the helical waveguide and a remaining wavepacket in the free waveguide. (c) Spin-dependent dispersion relations of a helical waveguide. The initial wavenumber k_0 and energy E_0 of an input state are marked by a green circle. The difference between the input wavenumber k_0 and spin-dependent wavenumbers $k_\uparrow$ and $k_\downarrow$ of the E_0-energetically resonant eigenstates of the helical waveguide are highlighted by red and blue arrows, respectively.

dynamics can then be described by an effective one-dimensional quantum state in the form $\psi_\uparrow(s, t)|\uparrow\rangle + \psi_\downarrow(s, t)|\downarrow\rangle$, where $|\uparrow\rangle$ and $|\downarrow\rangle$ are the eigenstates of the Pauli matrix σ_z, t is the time coordinate, and s represents the position on the helical path, as shown in Figure 1a. As in previous CISS models,[21−23,25,26,29] we assume that the electric field induced by the molecule is helical-symmetric and that the field on the helical path is oriented in the normal direction, $\mathbf{E} = E\mathbf{e}_N(s)$ with constant E, where the normal unit vector $\mathbf{e}_N(s)$ depends on the position s. The dynamics of the electron wavepacket is governed by an effective Hamiltonian[33] of the form

$$H_h = \frac{p_s^2}{2m_h} + U_h + \frac{\alpha}{2}\{\boldsymbol{\sigma}\cdot\mathbf{e}_B(s), p_s\} \tag{1}$$

where $p_s = -i\hbar\partial_s$ is the momentum operator in the tangential direction $\mathbf{e}_T(s)$, $m_h = 10\ m_e$ is the effective electron mass[34,35] with m_e its rest mass, and U_h is a constant potential energy shift. The anticommutator term in eq 1 represents the spin−orbit interaction, which is generally described by $H_{SOC} = -\boldsymbol{\sigma}\cdot(\boldsymbol{\alpha}\times\mathbf{p})$, where $\boldsymbol{\alpha}$ is proportional to $\mathbf{E}$ and quantifies the SOC strength via its magnitude α. Thus, since we assume $\mathbf{E}$ parallel to $\mathbf{e}_N(s)$, we have $\boldsymbol{\alpha} = \alpha\mathbf{e}_N(s)$ and H_{SOC} as shown in eq 1.

As shown in the Supporting Information, the eigenstates as a function of the helical position coordinate s can be expressed as

$$\langle s|k, \pm\rangle = \frac{A_\pm e^{ik_\uparrow s}|\uparrow\rangle + e^{ik_\downarrow s}|\downarrow\rangle}{\sqrt{2\pi(1 + |A_\pm|^2)}} \tag{2}$$

with $D = \sqrt{R^2 + P^2}$, where the spin-dependent wavenumbers are given by $k_\uparrow = k - (2D)^{-1}$ and $k_\downarrow = k + (2D)^{-1}$, and A_+ and A_- are k-independent coefficients. This shows that there are two distinct groups of eigenstates, $\{|k, +\rangle\}$ and $\{|k, -\rangle\}$, with different energies and opposite spin polarizations $P_\pm = \langle\sigma_z\rangle = (|A_\pm|^2 - 1)/(|A_\pm|^2 + 1)$ which fulfill $P_+ = -P_-$. In Figure 1c, the dispersion relation between energy $E(k, +)$ and wavenumber $k_\uparrow$ (or $k_\downarrow$) of the eigenstates $\{|k, +\rangle\}$ is shown in a red (or blue) solid line, where $U_h = 0.9$ eV and $\hbar\alpha = 10$ meV nm are considered as an example. These $k_\uparrow$ and $k_\downarrow$ curves differ due to the correlations between spin states and wavenumbers induced by spin−orbit interaction, as shown in eq 2. Similarly, the two components of the dispersion relation of the $\{|k, -\rangle\}$ eigenstates are shown in red and blue dashed lines, respectively, in Figure 1c. These results demonstrate that when an electron with well-defined energy E_0 and wavenumber k_0 enters a helical waveguide in such a way that the energy of an electron wavepacket is conserved (such that $E_0 = E(k, \pm)$), the wavenumber $k_\uparrow$ or $k_\downarrow$ of the helical eigenstate $|k, \pm\rangle$ will generally differ from k_0 of the input state. Importantly, the difference between wavenumbers can be smaller or larger depending on the incoming state's polarization. In the case shown in Figure 1c, the difference is smaller for a spin-up state than for a spin-down state, $|k_0 - k_\uparrow| < |k_0 - k_\downarrow|$, as highlighted by red and blue arrows. Therefore, if the transition probability favors smaller differences between wavenumbers—that is, if momentum conservation is (at least partially) enforced—then a $|\uparrow\rangle$ state will transition to the helix more readily than a $|\downarrow\rangle$ state. As we will show shortly, this partial momentum conservation does indeed arise when the interfacial coupling is extended over a region rather than being point-like, thus constituting the centerpiece of our model. Finally, it follows from these preliminaries that an initially unpolarized mixed state will lose $|\uparrow\rangle$ population to the helix more quickly than $|\downarrow\rangle$: This results in a net negative spin polarization of the remaining electronic density that has not been transmitted to the helix, an effect which can be further amplified by repeated interactions with other helices.

To quantitatively model the relation between interfacial structure and momentum-conservation assisted spin filtering, we introduce a second one-dimensional waveguide. This second waveguide shall be governed by a free-space Hamiltonian in the form $H_f = (2m_e)^{-1}p_q^2$, where $p_q = -i\hbar\partial_q$ is the momentum operator along a separate coordinate q, as shown in the inset of Figure 1(b). The eigenstates of H_f are spin-independent and given by $\langle q|k\rangle = (2\pi)^{-1/2}e^{ikq}$ with wavenumbers k (and $\langle s|k\rangle = 0$). We call this the *free waveguide* or free-space channel, as opposed to the helical waveguide. To model an interwaveguide scattering process occurring over an extended region, we consider coupling between free (coordinate q) and helical waveguides (s) of the form

$$V(s, q) = V_0 \exp\left(-\frac{(s - s_0)^2}{2\xi^2}\right)\delta((s - s_0) - (q - q_0)) \tag{3}$$

https://doi.org/10.1021/acs.jpclett.1c03975
J. Phys. Chem. Lett. 2022, 13, 1791−1796

where s and q denote the position on the helical and free waveguide, respectively and $\delta(x)$ is the Dirac delta, which signifies that each position is coupled to exactly one position on the opposite waveguide. Later, we will discuss a more realistic extension of this simplified coupling model. This $V(s, q)$ implies that when an electron wavepacket propagates in the free waveguide, the phase information on the input state, encoded as a function of the free-space coordinate q, is transferred to the helical waveguide over an extended width ξ of the interface centered at $(s, q) = (s_0, q_0)$, as shown schematically in the inset to Figure 1b. When the input state of the free-space channel is a $|\uparrow\rangle$ state with wavenumber k_0, the coupling to a helical eigenstate $|k, \pm\rangle$ is given by

$$|\langle k, \pm|V|k_0, \uparrow\rangle|^2 = \left(\frac{V_0^2\xi^2}{2\pi}\frac{|A_\pm|^2}{1+|A_\pm|^2}\right)e^{-\xi^2(\Delta k)^2} \tag{4}$$

with $\Delta k = k_\uparrow - k_0$. We see that the coupling strength is stronger if the eigenstate $|k, \pm\rangle$ has a larger $|\uparrow\rangle$ component amplitude $|A_\pm|$ (cf. eq 2). However, more importantly, as the width ξ of the interface increases, the effective coupling strength becomes more sensitive to the momentum mismatch $\hbar\Delta k$, and as a result transfer occurs only if the wavenumber is conserved, $k_\uparrow \approx k_0$. On the other hand, when the interface is very narrow, $\xi \to 0$, the effective coupling strength becomes independent of Δk. In this case, the only information provided to a helical channel is the time-dependent amplitude of the input state at a single-point contact with the free waveguide. This makes scattering probabilities independent of changes in momentum, similar to the textbook problem of one-dimensional scattering at a step potential.[36]

To demonstrate that a nonzero length ξ of the interface can induce the momentum-conservation assisted spin filtering, we consider a Gaussian initial electron state in the form

$$\langle q|\psi_i^\sigma(t=0)\rangle = \frac{1}{\pi^{1/4}\zeta^{1/2}}\exp\left(-\frac{(q-q_i)^2}{2\zeta^2} + ik_0q\right)|\sigma\rangle \tag{5}$$

with $\sigma \in \{\uparrow, \downarrow\}$, and with an initial center position q_i such that the amplitude at the interface around q_0 is negligible. This is a superposition of the eigenstates $|k\rangle$ of the free-space Hamiltonian H_f such that $|\langle k|\psi_i^\sigma\rangle|^2 \propto e^{-(k-k_0)^2\zeta^2}$, which is centered at $\langle k\rangle = \langle p\rangle/\hbar = k_0$ with an uncertainty $\sigma_k = (\sqrt{2}\zeta)^{-1}$ (we use $\zeta = 100/k_0$ throughout). We can then apply time-dependent perturbation theory to first order in V (eq 3), similar to Fermi's Golden Rule, to obtain the probability that an incoming Gaussian state $|\psi_i^\sigma\rangle$ of polarization σ, eq 5, has transitioned to a helix eigenstate $|k_{out}, \pm\rangle$, eq 2, in the long-time limit $t \to \infty$ (see Supporting Information for further details):

$$\lim_{t\to\infty}|\langle k_{out}, \pm|\psi_i^\sigma(t)\rangle|^2 \propto \left|\int_{\mathbb{R}} e^{-\xi^2(\Delta k)^2/2-\zeta^2(k-k_0)^2/2-i\phi(k)}\delta(\omega(k))\,dk\right|^2 \tag{6}$$

Here, $\Delta k = k_{out} - \sigma/(2D) - k$ and $\omega(k) = \hbar k^2/(2m_e) - E(k_{out}, \pm)/\hbar$, and $\phi(k) = (q_i - q_0)k$ is a (largely irrelevant) phase. We see that, in the long-time limit, energy is rigorously conserved during transitions, but momentum is only loosely conserved according to a Gaussian law, as predicted by eq 4. For small ξ and/or V_0, such that the influence of $V(s, q)$ remains perturbative, this simple equation can be used to accurately describe the transition probabilities and therefore the spin polarizations of our model. We quantify the spin polarization arising from an initially unpolarized mixed state $\rho_0 = \frac{1}{2}[|\psi_i^\uparrow\rangle\langle\psi_i^\uparrow| + |\psi_i^\downarrow\rangle\langle\psi_i^\downarrow|]$ with $|\psi_i^\sigma\rangle$ from eq 5 as

$$P_1 = \mathrm{Tr}\{[\mathcal{P}_f\rho_1\mathcal{P}_f^\dagger]\sigma_z\}/\mathrm{Tr}\{\mathcal{P}_f\rho_1\mathcal{P}_f^\dagger\}$$

where ρ_1 is the state ρ_0 after passing through an interaction region with a helix, and $\mathcal{P}_f$ is the projector onto the free-waveguide component. The polarization P_n after n repeated interactions with separate helices is defined analogously using the state ρ_n, which is the result of scattering the state $\mathcal{P}_f\rho_{n-1}\mathcal{P}_f^\dagger$.

To expand our analysis to the nonperturbative regime, we calculate numerically the dynamics of the wavepacket using a standard finite-difference scheme (see Supporting Information), which further shows good agreement with eq 6 within the perturbative regime. We illustrate the rich physics of our model by demonstrating the effect of varying the interfacial length ξ and the incoming momentum $\hbar k_0$: In Figure 2a, the dispersion relations of the spin components of the helical eigenstates $|k, \pm\rangle$ are shown in red and blue, in addition to that of the free-space eigenstates, shown in black. The dispersion curves are crossed at four different wavenumbers $k_{1,2,3,4}$, highlighted by green arrows. In Figure 2b, where $\hbar\alpha = 10$ meV nm and $V_0 = 10$ meV, the spin polarization P_1 after a single scattering event is shown as a function of the input wavenumber k_0 and the width ξ of the Gaussian coupling spectrum of the interface. As expected from the above discussion, the spin polarization is zero for $\xi = 0$ (single-point coupling) and the spin polarization effect is enhanced as ξ increases. At the crossing point of the momenta $k_{1,3}$ ($k_{2,4}$), the spin polarization becomes maximally positive (negative), as these momenta correspond to the $|\downarrow\rangle$ ($|\uparrow\rangle$) component of the helical eigenstates, causing an incoming $|\downarrow\rangle$ ($|\uparrow\rangle$) state to be transmitted to the helix with higher probability, as predicted by eq 6. In Figure 2c, where $\xi = 1$ nm and $k_0 \approx 5$ nm^{-1}, the spin polarization is displayed as a function of the interfacial coupling strength V_0 for different spin−orbit coupling strengths from 0.1 meV nm to 10 meV nm. For V_0, we considered a range of 10−100 meV which is similar to that for typical molecule-lead hopping integrals.[21,37,38] Inside the interface, the wavepacket undergoes interwaveguide Rabi oscillations whose frequencies depend on V_0. Since the wavepacket stays within the interface region for a finite time that is determined by its group velocity, the transmission to the helix is maximized when the duration of the scattering is a half period of the Rabi oscillations. This is the case when $V_0 = 70$ meV (see Supporting Information for more details). It is notable that even for weak spin−orbit coupling $\hbar\alpha = 0.1$ meV nm and 1 meV nm, the spin polarization reaches values up to ∼2% and ∼22%, respectively. Figure 2d shows the results of numerical simulations (shown as dots) with $V_0 = 40$ meV demonstrating that the spin polarization is further enhanced when the input wavepacket is scattered multiple times by independent helices. In simulations, the distance between neighboring helices is taken to be sufficiently large compared to the width of the wave packet in the straight waveguide so that the electron is scattered independently at each helix. For example, in the case of weak spin−orbit coupling strength $\hbar\alpha = 1$ meV nm, the spin polarization is increased from $P_1 \approx 6\%$ to $P_{10} \approx 43\%$ after 10 consecutive scattering events.

https://doi.org/10.1021/acs.jpclett.1c03975
J. Phys. Chem. Lett. 2022, 13, 1791−1796

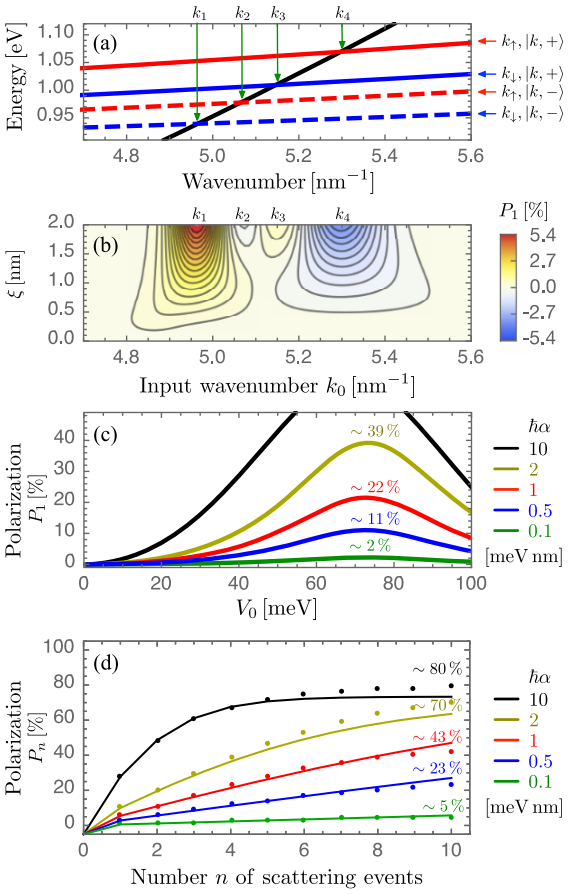

Figure 2. (a) Spin-dependent dispersion relations of a helical molecule (red and blue, cf. Figure 1c), and the free-space dispersion relation (black), for U_h = 0.9 eV and $\hbar\alpha$ = 10 meV nm. The $k_{1,2,3,4}$ of the four crossing points are highlighted by green arrows. (b) Spin polarization P_1 after a single scattering event as a function of input wavenumber k_0 and the interaction region width ξ (cf. Figure 1b). U_h and α as in part a, with V_0 = 10 meV. (c) P_1 as a function of the interfacial coupling strength V_0 for ξ = 1 nm. We use k_0 = 5.075 nm^{-1} except for $\hbar\alpha$ = 10 meV nm, where 4.975 nm^{-1} is considered due to the α-dependence of the crossing points. (d) Spin polarization P_n after n scattering events with parameters as given in part c and V_0 = 40 meV. Dots are numerical calculations, and solid lines are transfer-matrix-based extrapolations.

Furthermore, using a transfer-matrix-like method, we can estimate the n-scattering polarization P_n based only on the single-scattering data, which also shows that $|P_\infty|<$ 100% is caused by spin-flip back-transfer from the helical to straight waveguide (solid lines in Figure 2d; see Supporting Information for details). These results demonstrate that high spin polarization can be obtained from initially unpolarized electrons when scattering occurs over an extended region of a helical molecule even for weak intrinsic SOC strength ($\hbar\alpha \lesssim$1 meV nm).

Notice that the vanishing spin polarization in the case of single-point couplings is in line with the well-known fact that, in one-dimensional theories, spin−orbit coupling can be removed by a unitary transformation and hence—on its own—cannot account for spin-filtering.[39] Previous studies have therefore claimed that multiple channels such as additional helix strands[38,40] or orbitals[23,41] are required to observe spin polarization. As shown in the Supporting Information, the extended nature of the interface coupling prevents spin-dependence in our model from being removed by a unitary transformation and no intramolecular multichannel structure need be employed.

The mechanism of momentum conservation and spin-dependent transmission can also be used to understand spin-polarized transport through a helical waveguide attached to leads: Figure 3a illustrates a three-terminal setup with an

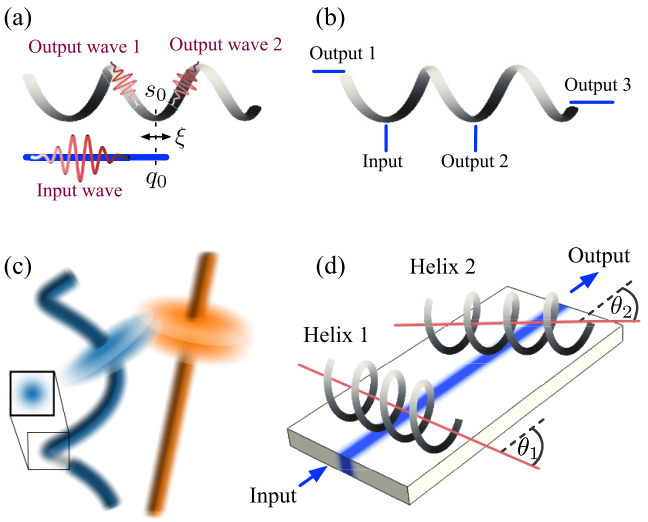

Figure 3. (a) Three-terminal setup where the tip of an electrode is coupled to a single helix over an extended region. An unpolarized input wavepacket is transmitted to the helix and results in oppositely polarized wavepackets traveling in opposite directions. (b) In a general N-terminal setup, where all interfaces are point contacts, no spin polarization can be observed. (c) To incorporate geometrical effects, an interwaveguide coupling matrix is calculated from the overlap between Gaussian cross-section slices: One slice-wedge pair is shown exploded. (d) Schematic representation of multiple scattering events with varying orientations of the helix axes. Helix 2 is shown in the locally parallel configuration $\theta_2 \approx 52°$, whereas helix 1 is not.

electrode tip coupled to a helix over a length ξ. A wavepacket transmitted to the helix splits into oppositely polarized wavepackets propagating in opposite directions inside the helix. In this case—as well as in any general N-terminal setup as depicted in Figure 3b—average spin polarization vanishes if all couplings are point contacts.

Last, the coupling function $V(s, q)$ of eq 3 may be a simplification of the interwaveguide coupling, as it does not directly depend on the 3D arrangement of the system. Therefore, to further validate our interface-based mechanism and test its robustness against disorder, we have calculated dynamics using a more elaborate coupling function $V(s, q)$ based on the 3D overlap between Gaussian cross-section wave functions occupying the straight and helical systems, as illustrated in Figure 3c. This more advanced coupling model naturally depends on the angle and distance between the helix and the straight waveguide, and it is also no longer diagonal in the sense that $V = 0$ does not necessarily hold for $s - s_0 \neq q - q_0$. Using this geometry-dependent model, we examine the influence of variations of the angle to the helix, illustrated in Figure 3d. The simpler coupling model of eq 3 is closest to the geometrical configuration in which the tangent vectors of the two waveguides are parallel at their point of least separation, given by $\theta = \arccos(P/D) \approx 52°$: We find that variations of ±20° about this angle have little impact on the spin selectivity

https://doi.org/10.1021/acs.jpclett.1c03975
J. Phys. Chem. Lett. 2022, 13, 1791−1796

(shown in Supporting Information). We therefore conclude that our model is sufficiently robust against static disorder to be measurable in experimental setups similar to those proposed here.

In conclusion, using a simple model consisting of a straight electron waveguide coupled to a helical waveguide, we have shown that electron wavepackets can become strongly polarized due to spin-dependent transmission when the interwaveguide coupling is extended over a region of nonzero length. A multichannel structure of the helical molecule is not required. These effects are robust against static disorder and can be enhanced by consecutive helix interactions. By quantitatively investigating the relationship between the coupling region width and the spin polarization, we identified interface-induced (partial) conservation of momentum as a crucial ingredient to this manifestation of CISS, pointing us to an intuitive and well-established principle to guide further studies of spin selectivity. This complements existing work on interface design in CISS experiments[42] by providing a directly deducible and simple mechanism without the need to invoke further phenomena such as dephasing. This mechanism is found to arise naturally in the continuum case, and further analysis may reveal how our findings are changed when considering a discretized tight-binding case or how the principle of momentum conservation could be applied to setups involving transport through helical molecules. Furthermore, our findings can be investigated experimentally using a setup as shown in Figure 3d with waveguides or leads of varying thickness representing different interface widths. Our results demonstrate that an achiral system can show CISS effects mediated by an interfacial coupling to helical systems. These findings may be related to experimental observations of induction of chirality where achiral nanostructures exhibit chiral properties once adsorbed by helical molecules.[43−48]

■ ASSOCIATED CONTENT

Supporting Information

The Supporting Information is available free of charge at https://pubs.acs.org/doi/10.1021/acs.jpclett.1c03975.

Helix Hamiltonian eigenstates and single-channel single-helix dynamics, spin removal via gauge transformations in one-channel setups, the numerical method, coupling-strength dependence of polarization, transfer-matrix extrapolation method for multiple scatterings, wave function-overlap-based estimation of interwaveguide coupling matrix, and perturbation theory treatment (PDF)

■ AUTHOR INFORMATION

Corresponding Author

Martin B. Plenio − *Institut für Theoretische Physik und IQST, Universität Ulm, D-89081 Ulm, Germany*; Email: martin.plenio@uni-ulm.de

Authors

Clemens Vittmann − *Institut für Theoretische Physik und IQST, Universität Ulm, D-89081 Ulm, Germany*; orcid.org/0000-0003-1243-0756

R. Kevin Kessing − *Institut für Theoretische Physik und IQST, Universität Ulm, D-89081 Ulm, Germany*; orcid.org/0000-0001-9614-4778

James Lim − *Institut für Theoretische Physik und IQST, Universität Ulm, D-89081 Ulm, Germany*

Susana F. Huelga − *Institut für Theoretische Physik und IQST, Universität Ulm, D-89081 Ulm, Germany*

Complete contact information is available at: https://pubs.acs.org/10.1021/acs.jpclett.1c03975

Notes

The authors declare no competing financial interest.

■ ACKNOWLEDGMENTS

This work was supported by the ERC Synergy grant HyperQ (Grant No. 856432). The authors acknowledge support by the state of Baden-Württemberg through bwHPC and the German Research Foundation (DFG) through Grant No. INST 40/575-1 FUGG (JUSTUS 2 cluster).

■ REFERENCES

(1) Aiello, C. D.; Abbas, M.; Abendroth, J.; Banerjee, A. S.; Beratan, D.; Belling, J.; Berche, B.; Botana, A.; Caram, J. R.; Celardo, L. et al. A Chirality-Based Quantum Leap: A Forward-Looking Review.*arXiv* 2020; arXiv:2009.00136.

(2) Naaman, R.; Waldeck, D. H. Spintronics and Chirality: Spin Selectivity in Electron Transport Through Chiral Molecules. *Annu. Rev. Phys. Chem.* **2015**, *66*, 263−281.

(3) Göhler, B.; Hamelbeck, V.; Markus, T. Z.; Kettner, M.; Hanne, G. F.; Vager, Z.; Naaman, R.; Zacharias, H. Spin Selectivity in Electron Transmission Through Self-Assembled Monolayers of Double-Stranded DNA. *Science* **2011**, *331*, 894−897.

(4) Kettner, M.; Göhler, B.; Zacharias, H.; Mishra, D.; Kiran, V.; Naaman, R.; Fontanesi, C.; Waldeck, D. H.; Sęk, S.; Pawłowski, J.; et al. Spin Filtering in Electron Transport Through Chiral Oligopeptides. *J. Phys. Chem. C* **2015**, *119*, 14542−14547.

(5) Mishra, D.; Markus, T. Z.; Naaman, R.; Kettner, M.; Gohler, B.; Zacharias, H.; Friedman, N.; Sheves, M.; Fontanesi, C. Spin-Dependent Electron Transmission Through Bacteriorhodopsin Embedded in Purple Membrane. *Proc. Natl. Acad. Sci. U.S.A* **2013**, *110*, 14872−14876.

(6) Carmeli, I.; Kumar, K. S.; Heifler, O.; Carmeli, C.; Naaman, R. Spin Selectivity in Electron Transfer in Photosystem I. *Angew. Chem., Int. Ed.* **2014**, *53*, 8953−8958.

(7) Niño, M.; Kowalik, I.; Luque, F.; Arvanitis, D.; Miranda, R.; De Miguel, J. Enantiospecific Spin Polarization of Electrons Photoemitted Through Layers of Homochiral Organic Molecules. *Adv. Mater.* **2014**, *26*, 7474−7479.

(8) Kettner, M.; Maslyuk, V. V.; Nürenberg, D.; Seibel, J.; Gutierrez, R.; Cuniberti, G.; Ernst, K.-H.; Zacharias, H. Chirality-Dependent Electron Spin Filtering by Molecular Monolayers of Helicenes. *J. Phys. Chem. Lett.* **2018**, *9*, 2025−2030.

(9) Xie, Z.; Markus, T.; Cohen, S.; Vager, Z.; Gutierrez, R.; Naaman, R. Spin Specific Electron Conduction Through DNA Oligomers. *Nano Lett.* **2011**, *11*, 4652−4655.

(10) Bostick, C. D.; Mukhopadhyay, S.; Pecht, I.; Sheves, M.; Cahen, D.; Lederman, D. Protein Bioelectronics: A Review of What We Do and Do Not Know. *Rep. Prog. Phys.* **2018**, *81*, 026601.

(11) Dor, O. B.; Yochelis, S.; Mathew, S. P.; Naaman, R.; Paltiel, Y. A Chiral-Based Magnetic Memory Device Without a Permanent Magnet. *Nat. Commun.* **2013**, *4*, 2256.

(12) Michaeli, K.; Varade, V.; Naaman, R.; Waldeck, D. H. A New Approach Towards Spintronics—Spintronics With No Magnets. *J. Phys.: Condens. Matter* **2017**, *29*, 103002.

(13) Mondal, P. C.; Fontanesi, C.; Waldeck, D. H.; Naaman, R. Spin-Dependent Transport Through Chiral Molecules Studied by Spin-Dependent Electrochemistry. *Acc. Chem. Res.* **2016**, *49*, 2560−2568.

(14) Yang, X.; van der Wal, C. H.; van Wees, B. J. Detecting Chirality in Two-Terminal Electronic Nanodevices. *Nano Lett.* **2020**, *20*, 6148−6154.
(15) Chiesa, A.; Chizzini, M.; Garlatti, E.; Salvadori, E.; Tacchino, F.; Santini, P.; Tavernelli, I.; Bittl, R.; Chiesa, M.; Sessoli, R.; et al. Assessing the Nature of Chiral-Induced Spin Selectivity by Magnetic Resonance. *J. Phys. Chem. Lett.* **2021**, *12*, 6341−6347.
(16) Kumar, A.; Capua, E.; Kesharwani, M. K.; Martin, J. M. L.; Sitbon, E.; Waldeck, D. H.; Naaman, R. Chirality-Induced Spin Polarization Places Symmetry Constraints on Biomolecular Interactions. *Proc. Natl. Acad. Sci. U.S.A* **2017**, *114*, 2474−2478.
(17) Banerjee-Ghosh, K.; Ben Dor, O.; Tassinari, F.; Capua, E.; Yochelis, S.; Capua, A.; Yang, S.-H.; Parkin, S. S. P.; Sarkar, S.; Kronik, L.; et al. Separation of Enantiomers by Their Enantiospecific Interaction With Achiral Magnetic Substrates. *Science* **2018**, *360*, 1331−1334.
(18) Metzger, T. S.; Mishra, S.; Bloom, B. P.; Goren, N.; Neubauer, A.; Shmul, G.; Wei, J.; Yochelis, S.; Tassinari, F.; Fontanesi, C.; et al. The Electron Spin as a Chiral Reagent. *Angew. Chem., Int. Ed.* **2020**, *59*, 1653−1658.
(19) Dianat, A.; Gutierrez, R.; Alpern, H.; Mujica, V.; Ziv, A.; Yochelis, S.; Millo, O.; Paltiel, Y.; Cuniberti, G. Role of Exchange Interactions in the Magnetic Response and Intermolecular Recognition of Chiral Molecules. *Nano Lett.* **2020**, *20*, 7077−7086.
(20) Kapon, Y.; Saha, A.; Duanis-Assaf, T.; Stuyver, T.; Ziv, A.; Metzger, T.; Yochelis, S.; Shaik, S.; Naaman, R.; Reches, M.; et al. Evidence for New Enantiospecific Interaction Force in Chiral Biomolecules. *Chem.* **2021**, *7*, 2787−2799.
(21) Gutierrez, R.; Díaz, E.; Naaman, R.; Cuniberti, G. Spin-Selective Transport Through Helical Molecular Systems. *Phys. Rev. B* **2012**, *85*, 081404.
(22) Guo, A.-M.; Sun, Q.-F. Spin-Dependent Electron Transport in Protein-Like Single-Helical Molecules. *Proc. Natl. Acad. Sci. U.S.A* **2014**, *111*, 11658−11662.
(23) Gutierrez, R.; Díaz, E.; Gaul, C.; Brumme, T.; Domínguez-Adame, F.; Cuniberti, G. Modeling Spin Transport in Helical Fields: Derivation of an Effective Low-Dimensional Hamiltonian. *J. Phys. Chem. C* **2013**, *117*, 22276−22284.
(24) Geyer, M.; Gutierrez, R.; Mujica, V.; Cuniberti, G. Chirality-Induced Spin Selectivity in a Coarse-Grained Tight-Binding Model for Helicene. *J. Phys. Chem. C* **2019**, *123*, 27230−27241.
(25) Naaman, R.; Paltiel, Y.; Waldeck, D. H. Chiral Molecules and the Electron Spin. *Nat. Rev. Chem.* **2019**, *3*, 250−260.
(26) Michaeli, K.; Naaman, R. Origin of Spin-Dependent Tunneling Through Chiral Molecules. *J. Phys. Chem. C* **2019**, *123*, 17043−17048.
(27) Fransson, J. Chirality-Induced Spin Selectivity: The Role of Electron Correlations. *J. Phys. Chem. Lett.* **2019**, *10*, 7126−7132.
(28) Dalum, S.; Hedegård, P. Theory of Chiral Induced Spin Selectivity. *Nano Lett.* **2019**, *19*, 5253−5259.
(29) Ghazaryan, A.; Paltiel, Y.; Lemeshko, M. Analytic Model of Chiral-Induced Spin Selectivity. *J. Phys. Chem. C* **2020**, *124*, 11716−11721.
(30) Geyer, M.; Gutierrez, R.; Cuniberti, G. Effective Hamiltonian Model for Helically Constrained Quantum Systems Within Adiabatic Perturbation Theory: Application to the Chirality-Induced Spin Selectivity (CISS) Effect. *J. Chem. Phys.* **2020**, *152*, 214105.
(31) Evers, F.; Aharony, A.; Bar-Gill, N.; Entin-Wohlman, O.; Hedegård, P.; Hod, O.; Jelinek, P.; Kamieniarz, G.; Lemeshko, M.; Michaeli, K.; et al. Theory of Chirality Induced Spin Selectivity: Progress and Challenges. *Adv. Mater.* **2022**, 2106629.
(32) Naaman, R.; Waldeck, D. H. Chiral-Induced Spin Selectivity Effect. *J. Phys. Chem. Lett.* **2012**, *3*, 2178−2187.
(33) Ortix, C. Quantum Mechanics of a Spin-Orbit Coupled Electron Constrained to a Space Curve. *Phys. Rev. B* **2015**, *91*, 245412.
(34) Ladik, J. The Energy Band Structure and Conduction Properties of DNA. *Int. J. Quantum Chem.* **1974**, *8*, 65−69.
(35) Maia, F. F.; Freire, V. N.; Caetano, E. W. S.; Azevedo, D. L.; Sales, F. A. M.; Albuquerque, E. L. Anhydrous Crystals of DNA Bases Are Wide Gap Semiconductors. *J. Chem. Phys.* **2011**, *134*, 175101.
(36) Shankar, R. *Principles of Quantum Mechanics*; 2nd ed.; Plenum Press: New York, 1994; Chapter 5, pp 167−175.
(37) Zelovich, T.; Kronik, L.; Hod, O. Molecule-Lead Coupling at Molecular Junctions: Relation between the Real- and State-Space Perspectives. *J. Chem. Theory Comput.* **2015**, *11*, 4861−4869.
(38) Sierra, M. A.; Sánchez, D.; Gutierrez, R.; Cuniberti, G.; Domínguez-Adame, F.; Díaz, E. Spin-Polarized Electron Transmission in DNA-Like Systems. *Biomolecules* **2020**, *10*, 49.
(39) Entin-Wohlman, O.; Aharony, A.; Utsumi, Y. Comment on "Spin-Orbit Interaction and Spin Selectivity for Tunneling Electron Transfer in DNA. *Phys. Rev. B* **2021**, *103*, 077401.
(40) Guo, A.-M.; Sun, Q.-F. Spin-Selective Transport of Electrons in DNA Double Helix. *Phys. Rev. Lett.* **2012**, *108*, 218102.
(41) Utsumi, Y.; Entin-Wohlman, O.; Aharony, A. Spin Selectivity Through Time-Reversal Symmetric Helical Junctions. *Phys. Rev. B* **2020**, *102*, 035445.
(42) Guo, A.-M.; Díaz, E.; Gaul, C.; Gutierrez, R.; Domínguez-Adame, F.; Cuniberti, G.; Sun, Q.-f. Contact Effects in Spin Transport Along Double-Helical Molecules. *Phys. Rev. B* **2014**, *89*, 205434.
(43) Zhang, W.; Banerjee-Ghosh, K.; Tassinari, F.; Naaman, R. Enhanced Electrochemical Water Splitting with Chiral Molecule-Coated Fe3O4 Nanoparticles. *ACS Energy Let* **2018**, *3*, 2308−2313.
(44) Ben Dor, O.; Yochelis, S.; Radko, A.; Vankayala, K.; Capua, E.; Capua, A.; Yang, S.-H.; Baczewski, L. T.; Parkin, S. S. P.; Naaman, R.; et al. Magnetization switching in ferromagnets by adsorbed chiral molecules without current or external magnetic field. *Nat. Commun.* **2017**, *8*, 14567.
(45) Ma, W.; Xu, L.; de Moura, A. F.; Wu, X.; Kuang, H.; Xu, C.; Kotov, N. A. Chiral Inorganic Nanostructures. *Chem. Rev.* **2017**, *117*, 8041−8093.
(46) Alpern, H.; Yavilberg, K.; Dvir, T.; Sukenik, N.; Klang, M.; Yochelis, S.; Cohen, H.; Grosfeld, E.; Steinberg, H.; Paltiel, Y.; et al. Magnetic-related States and Order Parameter Induced in a Conventional Superconductor by Nonmagnetic Chiral Molecules. *Nano Lett.* **2019**, *19*, 5167−5175.
(47) Naaman, R.; Paltiel, Y.; Waldeck, D. H. Chiral Induced Spin Selectivity Gives a New Twist on Spin-Control in Chemistry. *Acc. Chem. Res.* **2020**, *53*, 2659−2667.
(48) Alpern, H.; Katzir, E.; Yochelis, S.; Katz, N.; Paltiel, Y.; Millo, O. Unconventional superconductivity induced in Nb films by adsorbed chiral molecules. *New J. Phys.* **2016**, *18*, 113048.

https://doi.org/10.1021/acs.jpclett.1c03975
J. Phys. Chem. Lett. 2022, 13, 1791−1796